



Positioning cyanamide defects in g-C₃N₄: Engineering energy levels and active sites for superior photocatalytic hydrogen evolution

Jili Yuan^{a,1}, Xia Liu^{b,1}, Yanhong Tang^{a,*}, Yunxiong Zeng^c, Longlu Wang^c, Shuqu Zhang^c, Tao Cai^d, Yutang Liu^d, Shenglian Luo^c, Yong Pei^{b,*}, Chengbin Liu^{c,*}

^a College of Materials Science and Engineering, Hunan University, Changsha 410082, PR China

^b Key Laboratory of Environmentally Friendly Chemistry and Applications of Ministry of Education, Xiangtan University, Xiangtan 411105, PR China

^c State Key Laboratory of Chemo/Biosensing and Chemometrics, Hunan University, Changsha 410082, PR China

^d College of Environment Science and Engineering, Hunan University, Changsha 410082, PR China

ARTICLE INFO

Keywords:

Graphitic carbon nitride
Cyanamide defects
Energy level engineering
Hydrogen evolution

ABSTRACT

g-C₃N₄ has recently emerged as a promising photocatalyst for solar energy conversion. Nonetheless, attempts to enhance its inherently low activity are rarely based on precise molecular tunability strategy. In this study, two-type cyanamide defects-grafting g-C₃N₄ (CCN) was prepared through the thermal polymerization of thiourea in the presence of KCl. Stable potassium isothiocyanate (KSCN) was in situ generated via thiourea isomerization and then reacted with different amino groups (–NH₂ and =NH) in tri-s-triazine rings to obtain two-type cyanamide defects. Theoretical calculations and experiment results confirm that the ratio of the two-type cyanamide defects could be adjusted by KCl dosage, accompanying tunable energy levels of CCN. The charge carrier transfer and separation of CCN was greatly improved. Furthermore, the existence of cyanamide defects hindered the formation of intermolecular hydrogen bonds among g-C₃N₄, which facilitated the formation of porous structure and exposed more active sites for photocatalytic hydrogen evolution reaction (HER). As a result, the optimized photocatalyst (CCN-0.03) showed a high HER rate of 4.0 mmol g^{−1} h^{−1}, which was 5 times higher than 0.8 mmol g^{−1} h^{−1} for pristine g-C₃N₄. And the apparent quantum efficiency reached up to 14.65% at 420 ± 10 nm. The findings deepen the understanding on precise molecular tuning of g-C₃N₄.

1. Introduction

Photocatalytic hydrogen evolution reactions (HER) from water provides a direct method to capture and store sunlight as chemical energy, and is a promising technology for solar energy conversion and storage [1–5]. The key to achieve solar hydrogen production is to develop chemically stable, high-efficiency and low-cost photocatalysts that are capable of working in visible light region and having appropriate energy levels stranding the redox potential for water splitting [6–9].

Graphitic carbon nitride (g-C₃N₄) as a metal-free photocatalyst is attracting wide-spread attention owing to its high physicochemical stability, adjustable electronic structure, and molecular tunability [10,11]. The g-C₃N₄ materials were commonly derived from thermal polymerization of urea, melamine, dicyanamide, or thiourea [12–14]. However, most of studies focused on optimizing poor solar light utilization [15–21], increasing surface area for more catalytic sites [22–24], surface modification [25], and composite formation with a (semi)

conductor [26]. While useful, there is striking lack of attempts to enhance the intrinsic activity of carbon nitrides [27]. Recently, the introduction of “defects” into the g-C₃N₄ framework has shown to significantly enhance the intrinsic activity of carbon nitrides on account of the molecule structure control. KSCN replaced the hydrogen on surface amino group of bulk g-C₃N₄ to introduce cyanamide defects that acted as coordinating group and related to catalytically relevant defect [28]. NaBH₄ modulated bulk g-C₃N₄ to produce nitrogen defects on the surface of g-C₃N₄ [29]. Alkali-assisted thermal polymerization introduced cyanamide defects into the nitrogen vacancies at –C–NH₂ position in g-C₃N₄, which could adjust band structures [30]. The hydrolyzation of cyanamide defects in HCl could form urea-modified g-C₃N₄ with relevant catalytic defect [31]. Nevertheless, these strategies to introduce defects into g-C₃N₄ framework required the assistance of chemical reagents or post-treatment. Meanwhile, it is difficult to selectively position cyanamide defects to g-C₃N₄ framework and the function of cyanamide defects at different chemical positions in g-C₃N₄ framework for photocatalytic activity is still unclear. Therefore, it is

* Corresponding authors.

E-mail addresses: tangyh@hnu.edu.cn (Y. Tang), ypnku78@gmail.com (Y. Pei), chem_cbliu@hnu.edu.cn (C. Liu).

¹ The authors contributed to the work equally.

desirable to develop a facile approach for in-situ introducing and positioning cyanamide defects into g-C₃N₄ during its synthesis, and necessarily expose the intrinsic function of cyanamide defects for photocatalytic activity.

Herein, we developed a precursor (thiourea) isomerization strategy to in-situ produce stable potassium isothiocyanate (KSCN) in the presence of KCl as nucleating agents. And then SCN[−] reacted with different amino groups (−NH₂ and =NH) in tri-s-triazine rings to obtain two-type cyanamide defects-grafting in g-C₃N₄ during thermal condensation of thiourea (containing SCN[−]). A “one stone, two birds” outcome was achieved by this strategy. Interestingly, the amount ratio of the two-type cyanamide defects could be facily adjusted by KCl dosage during thermal condensation of thiourea. Significantly, the band gap of cyanamide defects-grafting g-C₃N₄ (CCN) could be tuned by changing the amount ratio of the two-type cyanamide defects. In addition, the charge carrier transfer and separation of CCN was greatly improved due to the implantation of C≡N groups providing the ligating linkage to Pt active centers. Furthermore, the introduction of the two-type cyanamide defects hindered the formation of intermolecular hydrogen bonds among g-C₃N₄, broadening the distance between the molecule chains of g-C₃N₄, which facilitated the formation of porous structure, exposed more active sites for binding Pt, and thus enhanced photocatalytic H₂ evolution. The formation of CCN was illustrated as Scheme 1.

2. Experimental

2.1. Chemical materials

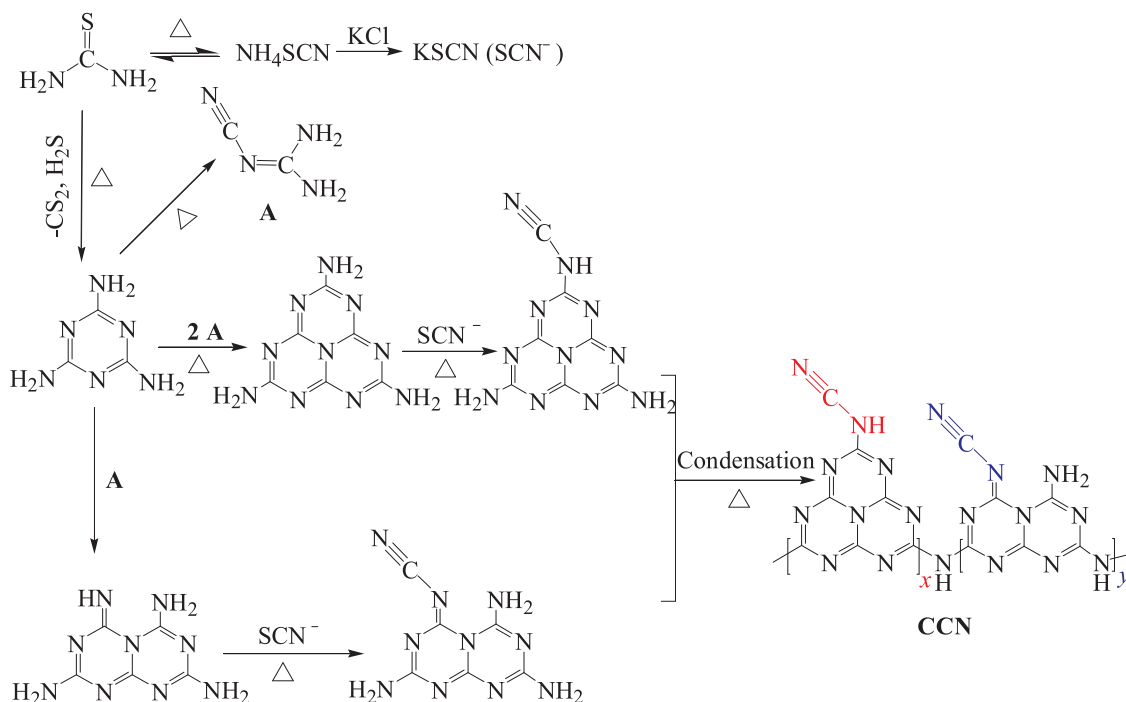
Nafion solution (5 wt%), NaSO₄, isopropanol, triethanolamine, thiourea, KCl, and chloroplatinic acid hexahydrate (> 99%, H₂PtCl₆·H₂O) were all obtained from Sinopharm Chemical Reagent Co. Ltd and used without further purification. Ultrapure (Milli-Q) water was used to prepare all solutions and in the photocatalytic hydrogen production tests.

2.2. Synthesis of g-C₃N₄ and CCN photocatalysts

Pristine g-C₃N₄ was prepared by thiourea thermal polymerization. Briefly, 10 g of thiourea was calcined at 600 °C in a tube furnace for 2 h at a heating rate of 2.5 °C min^{−1}. Cyanamide defects-grafting carbon nitride (CCN) were synthesized as follows: 10 g of thiourea was dissolved into aqueous KCl solutions (KCl 0.005, 0.01, 0.03, 0.05 and 0.1 g in 10 mL H₂O), the resulting solution was heated at 160 °C for 1 h, and the solution was rapidly frozen to −80 °C and kept for 4 h. The solid was then calcined in a tube furnace at 600 °C for 2 h at a heating rate of 2.5 °C min^{−1}. All samples were washed with deionized water to remove any residual alkali salt. The products were denoted as CCN-M (M = 0.005, 0.01, 0.03, 0.05 and 0.1 which corresponds to the mass (g) of KCl used).

2.3. Characterization

Powder X-ray diffraction (XRD) patterns were collected on a Bruker DAVINCI D8 ADVANCE diffractometer equipped with Cu-Kα source. The morphology of samples was examined using transmittance electron microscopy (TEM) (JEOL, JEM-2100F) and a field emission scanning electron microscope (SEM) (FEI XL-30E) at an accelerating voltage of 10 kV. Fourier transform infrared (FTIR) spectra were recorded on a Perkin Elmer GX spectrophotometer over the range 4000–400 cm^{−1}. Raman spectra were measured using an Advantage 200A Raman spectrometer with a 632.8 nm laser (Delta Nu, USA). Zeta potentials were measured on a Malvern Zetasizer Nano ZS. The C, N and O contents were measured via Vario EL III elemental analyzer. The chemical element compositions were also analyzed by the EDS mapping images captured on a Tecnai G2 F20 S-TWIN atomic resolution analytical microscope. Solid-state ¹³C magic angle spinning nuclear magnetic resonance (MAS NMR) spectra were recorded on a Bruker AVANCE III 400 MHz WB solid-state NMR spectrometer at room temperature. Diffuse reflectance spectra (DRS) were measured using a Cary 5000 spectrophotometer fitted with an integrating sphere attachment from 200 to 800 nm with BaSO₄ as the reference. X-ray photoelectron spectroscopy (XPS) measurements were performed on a Quantum 2000 Scanning ESCA Microprobe (Physical Electronics) using



Scheme 1. Schematic illustration of CCN formation.

monochromatic Al K α radiation (1486.7 eV) as the X-ray source. The specific surface area was determined by the Brunauer–Emmett–Teller (BET) method with N₂ adsorption at 77 K (BELSORP-mini II). The photoluminescence (PL) spectra were recorded with Hitachi F-7000 fluorescence spectrophotometer.

2.4. Photoelectrochemical measurements

The photoelectrochemical properties were investigated in a three-electrode cell by using an electrochemical analyzer (CHI Inc., USA). An ITO glass coated with catalyst, a Pt foil and a Ag/AgCl electrode in 0.5 M Na₂SO₄ aqueous solution (electrolyte) were used as the working electrode, the counter-electrode and the reference electrode, respectively. A 300 W Xe arc lamp equipped with a 420 nm cutoff filter was utilized as a light source. The electrochemical impedance spectra (EIS) were recorded at an applied potential of 1.0 V versus Ag/AgCl over the frequency range of 1 MHz to 0.01 Hz. The photocurrent with ON/OFF cycles was measured at an applied potential of 0 V vs. Ag/AgCl. Mott–Schottky plots were obtained under direct current potential polarization at different frequencies (1000, 1500 and 2000 Hz). The potential ranged from −0.4 to 1.6 V (vs. Ag/AgCl). For the fabrication of the photoanode, ITO were cleaned by ultrasonication in distilled water, absolute ethanol, and isopropanol for 15 min sequentially, and then dried in vacuum. 5 mg of photocatalysts and 10 μ L of Nafion solution (5 wt%) were dispersed in 1 mL water/isopropanol mixed solvent (3:1 v/v) by at least 30 min sonication to prepare a homogeneous catalyst colloid. Then, 110 μ L of the catalyst colloid was deposited onto the ITO conductive glass (active area of 3 cm²) and the catalyst on the ITO was 1.67 mg cm^{−2}. The catalyst-coated ITO was dried in air to form the working electrode.

2.5. Photocatalytic activity measurements

The photocatalytic H₂ production was carried out in a Pyrex glass reaction cell containing 80 mL 15 vol% of triethanolamine (TEOA) aqueous solution. 50 mg of photocatalysts were used in the reactor. 3 wt % Pt as the co-catalyst was in situ photodeposited on the surface of photocatalysts. Before the irradiation, the reaction cell was connected to a gas-closed system with a gas-circulated pump and evacuated several times to remove the air completely. A 300 W Xenon lamp equipped with a 420 nm cut-off filter was used as the visible-light source. The Xe lamp was positioned 20 cm away from the reactor where the focused intensity on the flask was 120 mW cm^{−2}. In a photocatalytic experiment, photocatalyst sample (50 mg) was dispersed in TEOA solution (15 vol%, 80 mL) or deionized water only (80 mL, 18.2 M Ω) for photocatalytic hydrogen evolution. The H₂ was analyzed by a gas chromatography (Shimadzu, GC2010) combined with 5 Å molecular sieve column (Plot Q column, 0.32 μ m) and high purity argon as carrier gas (99.999%).

2.6. Computational method and details

All calculations were performed within the framework of density functional theory (DFT) as implemented in the Vienna Ab initio Simulation Package (VASP). The exchange-correlation interactions were treated by generalized gradient approximation (GGA) parameterized by Perdew, Burke, and Ernzerhof (PBE). We described the interaction between ions and electrons using the projected augmented wave (PAW) with an energy cutoff of 500 eV. The atomic positions were optimized by the conjugate gradient algorithm until the force on each atom is less than 0.01 eV/Å. In calculating the density of state (DOS), the hybrid functional based on a screened Coulomb potential (HSE06) 77 was applied. The cell parameters (a, b, c) of g-C₃N₄ or CCN were fully relaxed. The Brillouin-zone was sampled by gamma-centered Monkhorst-Pack method with 3 \times 3 \times 5 k-point mesh for geometric optimizations and 5 \times 5 \times 7 k-point mesh for density of state

calculations.

2.7. Quantum efficiency calculation

The apparent quantum efficiency (AQE) for cyanamide defects-grafting carbon nitride was measured under the same photocatalytic reaction condition except that 100 mg of photocatalysts were used. The incident light was supplied by a 300 W Xe lamp with specific band-pass filters to get the desired incident wavelength (λ = 420, 450, 500, 550). The average intensity of irradiation was ca. 9.12 mW cm^{−2} and the irradiation area was ca. 12.56 cm². The quantum efficiency was calculated from Eqs. (1)–(5):

$$\text{AQE} [\%] = \frac{\text{Number of reacted electrons}}{\text{Number of incident photons}} \times 100\% \quad (1)$$

$$\frac{\text{Number of evolved hydrogen molecules} \times 2}{\text{Number of incident photons}} \times 100\% \quad (2)$$

$$\text{Number of evolved H}_2 \text{ molecules} = 2 \times M \times N_A \quad (3)$$

$$\text{Number of incident photons} = \frac{E\lambda}{hc} = \frac{S \times P \times \lambda}{hc} \quad (4)$$

$$\text{AQE} [\%] = \frac{2 \times M \times N_A \times h \times c}{S \times P \times \lambda \times t} \times 100\% \quad (5)$$

Where, M is the amount of H₂ molecules (mol), N_A is Avogadro constant (6.022 \times 10²³/mol), h is the Plank constant (6.626 \times 10^{−34} J s), c is the speed of light (3 \times 10⁸ m/s), λ is the wavelength of the monochromatic light (m), P is The average intensity of irradiation, S is the irradiation area (cm²), and t is the photoreaction time (s).

3. Results and discussions

The pristine g-C₃N₄ was prepared through the direct thermal polymerization of thiourea at 600 °C for 2 h in the absence of KCl. The CCN-M samples were prepared through the thermal polymerization of thiourea in the presence of KCl (M represented KCl dosage from 0.005 to 0.1 g during CCN preparation). X-ray diffraction (XRD) characterization was used to confirm the formation of g-C₃N₄. As shown in Fig. 1A, two typical diffraction peaks at 12.9° and 27.2° were ascribed to intralayer long-range atomic order (100) associated with the hydrogen bonds in g-C₃N₄ and interlayer periodic stacking (002) along the c-axis in g-C₃N₄, respectively [32–34]. The intensity of 12.9° peak became weak gradually with the increase of KCl dosage, indicative of reduced hydrogen bond effect in the intralayer of g-C₃N₄. The weakened hydrogen bond effect would disturb the periodic stacking of g-C₃N₄ sheets with the weakened intensity of the 27.2° peak. Fourier transform infrared (FTIR) spectra were used to further investigate the chemical structure evolution of CCN-M samples (Fig. 1B). All the g-C₃N₄ samples showed the out-of-plane bending mode of heptazine rings at 810 cm^{−1}, N–C=N hetero rings in the “melon” framework between 900 and 1800 cm^{−1}, and N–H stretching vibrations in 3000–3500 cm^{−1}. For the CCN samples, the intensity of the N–H stretching peak between 3000 and 3300 cm^{−1} gradually decreased with increasing KCl dosage, while a new peak at 2170 cm^{−1} appeared and became stronger with increasing KCl dosage, which corresponded to the asymmetric stretching vibration of cyano groups (C \equiv N) [35–37]. The results suggested that a replacement of the N–H groups by N–C \equiv N groups probably happened during the synthesis of CCN. As shown in Scheme 1, thiourea molecules could be reversibly isomerized to ammonium thiocyanate (NH₄SCN) upon heating (Fig. S1 in the Supporting information). When in the presence of KCl, the NH₄SCN was irreversibly transferred into potassium thiocyanate (KSCN), thus generating cyano group during thermal condensation of thiourea [38]. The titration reaction also confirmed the production of KSCN using Fe³⁺ as the probe of SCN[−] (Fig. S2). The Raman spectra also showed the stretch

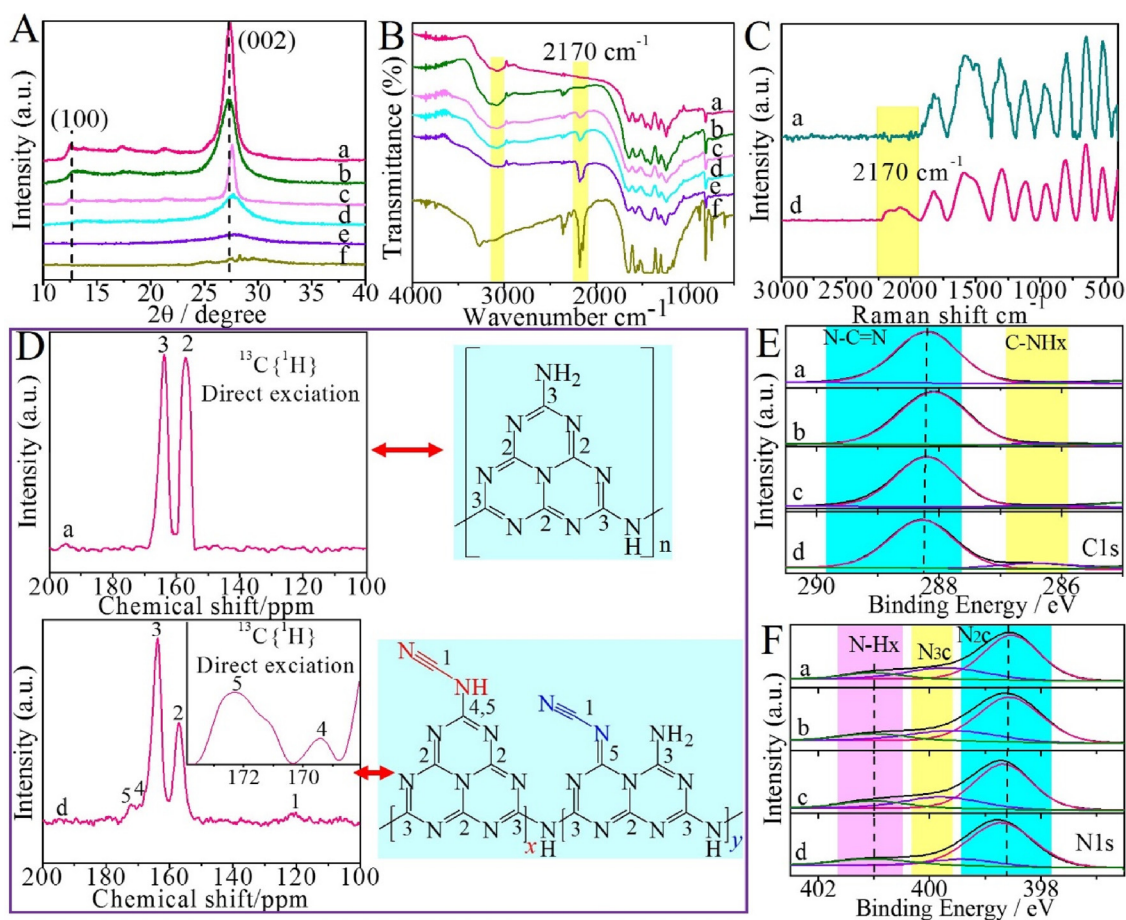


Fig. 1. (A) XRD patterns, (B) FTIR spectra, (C) Raman spectra, (D) solid-state ¹³C MAS NMR spectra, and XPS spectra of (E) C1s and (F) N1s: pristine g-C₃N₄ (a), CCN-0.005 (b), CCN-0.01 (c), CCN-0.03 (d), CCN-0.05 (e), and CCN-0.1 (f).

vibration of C≡N at 2170 cm⁻¹ for CCN samples (Fig. 1C) [39]. Solid-state ¹³C magic angle spinning (MAS) NMR measurements were conducted to reveal the structure of cyano groups (Fig. 1D). The NMR spectra of pristine g-C₃N₄ and CCN-0.03 showed two strong peaks at 157 and 163.8 ppm corresponding to the chemical shifts of C2 and C3 in the heptazine units, respectively [40]. Besides the new peak at 120.6 ppm of C1 in C≡N [41], other two new peaks of C4 at 169.3 ppm and C5 at 172 ppm were observed for CCN-0.03 [28,42]. Compared to the chemical shift (163.8 ppm) of C3 in pristine g-C₃N₄, the chemical shift of C4 and C5 in CCN-0.03 shift to 169.3 and 172 ppm, respectively, indicating the decrease of electron cloud densities in C4 and C5 due to the introduction of electron-drawing groups. It can be inferred that two-type cyanamide defects (–HN–C≡N and =N–C≡N) were positioned at C4 and C5 in CCN, respectively. It was also observed that the peak intensity of C2 decreased while that of C5 increased when KCl dosage increased (Fig. S3). And the molar ratios of C3/C2 and C5/C4 increased from 1.3 and 0.2 for CCN-0.005 to 1.9 and 5.1 for CCN-0.03, respectively (Table S1). The results indicated that the content of =N–C≡N cyanamide defect increased with increasing KCl dosage. The changes of functional groups were further investigated by X-ray photoelectron spectroscopy (XPS) analysis (Fig. 1E and F). And the quantified data are listed in Table S2. The ratio of NHx/C decreased a little due to the displacement of N–H by N–C≡N when introducing KCl.

In addition, there were very small O1s peaks in the XPS survey spectra of g-C₃N₄ and CCN, likely due to surface adsorbed adventitious oxygen-containing species (Fig. S4) [43,44]. All elements were quantified by organic elemental analysis (OEA) and XPS (Table S3). The N/C atomic ratios for CCN samples were close to that for pristine g-C₃N₄. The results indicated that the introduction of cyano groups did not

destroy the structure of g-C₃N₄ framework [45].

Based on the analysis above, more amine terminals in g-C₃N₄ were replaced by cyano terminals using more KCl dosage. And the introduction of cyano terminals hindered the formation of hydrogen bonds among g-C₃N₄ units [46,47]. Breaking hydrogen bonds greatly reduced the intermolecular force among g-C₃N₄ units, thus changing the morphology/texture of the carbon nitride as demonstrated by transmission electron microscopy (TEM) images in Fig. 2A, and scanning electron microscopy (SEM) images in Fig. S5. Compared to the smooth surface of pristine g-C₃N₄, there were pores in CCN samples, which became larger with increasing KCl dosage. In addition, the pores were also generated with the leaving of excess KCl during water-washing process. Both g-C₃N₄ and the CCN samples possessed mesoporous structures, however, the porous CCN samples showed smaller specific surface areas than pristine g-C₃N₄ (Fig. S6A and B, Table S4). The results indicated that the CCN samples had less adsorption sites towards N₂ than pristine g-C₃N₄, due to the more negative surface potential of the CCN samples (Fig. S7), which would repel N₂ with lone pair electrons.

The introduction of cyano groups into g-C₃N₄ obviously changed their optical properties and light harvesting ability. The CCN powders gradually became dark in color with increasing KCl dosage (top photographs, Fig. 2B). And the absorption edges of UV–vis diffuse reflectance spectra (DRS) occurred red shift with increasing KCl dosage (bottom, Fig. 2B), possibly due to the extended conjugation length after introducing conjugated cyano groups which replaced amino groups at edges. To explain the narrower bandgap in the CCN powders, conduction band (CB) by Mott-Schottky and valence band (VB) by XPS were collected (Fig. 2C and D). The CB potentials determined in the Mott-

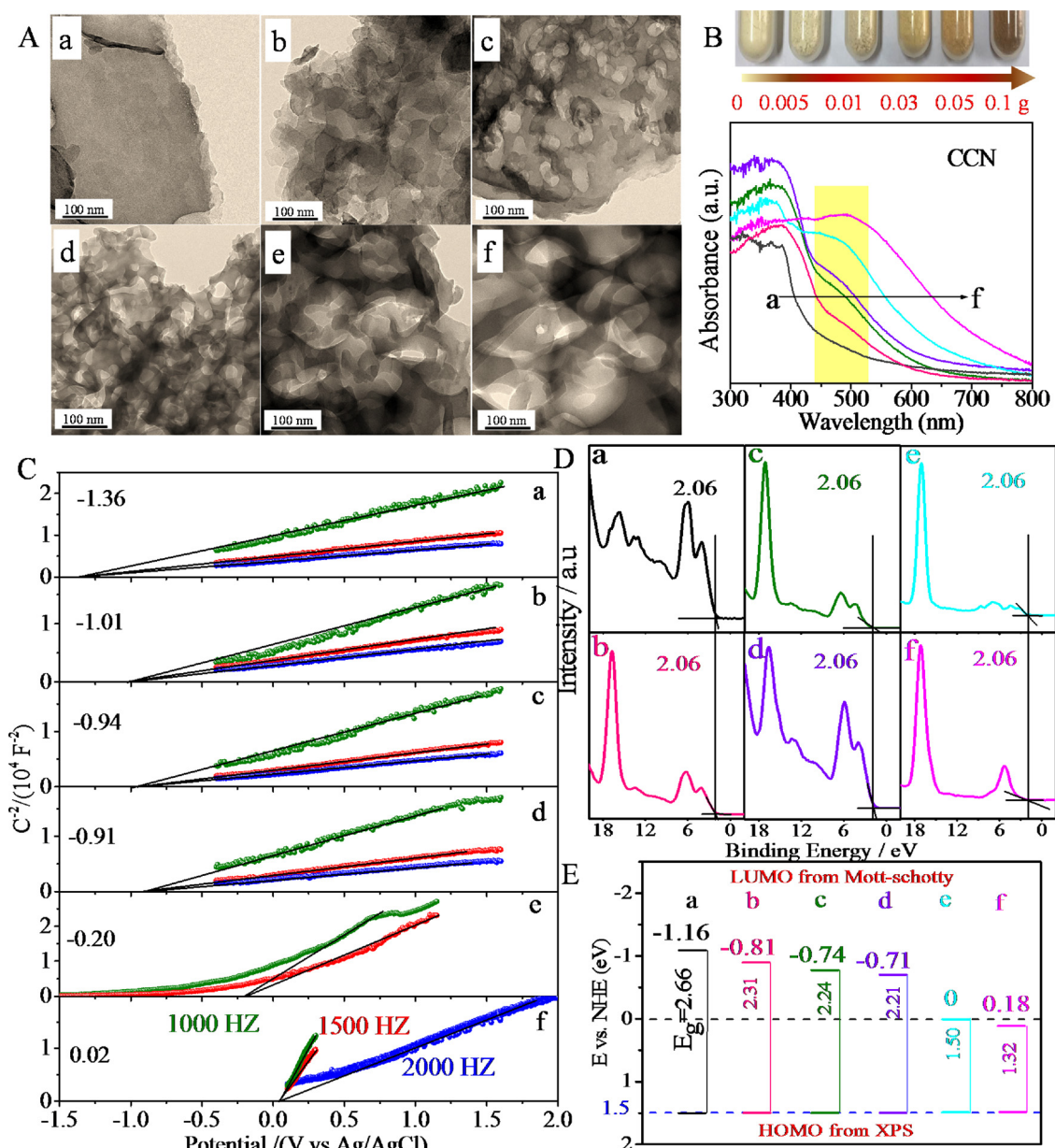


Fig. 2. (A) TEM images, (B) photographs (top) and UV-vis DRS spectra (bottom), (C) plots of transformed Mott-Schottky function versus photon energy, (D) VB-XPS spectra, and (E) band energy levels of the as-synthesized samples. (a) pristine g-C₃N₄, (b) CCN-0.005, (c) CCN-0.01, (d) CCN-0.03, (e) CCN-0.05, and (f) CCN-0.1.

Schottky plot of the pristine g-C₃N₄ CCN-0.005, CCN-0.01, CCN-0.03, CCN-0.05 and CCN-0.1 were about -1.36 , -1.01 , -0.94 , -0.91 , -0.20 and -0.02 V vs. Ag/AgCl (-1.16 , -0.81 , -0.74 , -0.71 , 0 and 0.18 V vs. normal hydrogen electrode (NHE)), respectively (Fig. 2C). In addition, both pristine g-C₃N₄ and CCN samples exhibited positive slopes in the Mott-Schottky plots at frequencies of 1.0, 1.5, and 2.0 kHz, indicative of n-type characteristic of semiconductors [48–50]. The Mott-Schottky plot slopes of the CCN samples tapered off compared to pristine g-C₃N₄, indicating that the electron donor density of the samples increased gradually with increasing cyano content in CCN. Higher donor density is very helpful for improving photocatalytic performance because of the increased electrical conductivity and the mobility of charge carriers [51].

The maximum VB values obtained by XPS were very close for pristine g-C₃N₄ and CCN samples (ca. 2.06 eV) (Fig. 2D). The VB was estimated to be ca. 1.50 eV vs. NHE according to the calculated contact potential difference between the samples and the analyzer at pH 7 using the formula $E_{\text{NHE}}/V = \Phi + 2.06 \text{ eV} - 4.44$ (E_{NHE} : potential of normal

hydrogen electrode; Φ of 3.88 eV: the electron work function of the analyzer) [6,52,53]. These results indicated that the introduction of cyano groups had significant effect on the CB energy level in CCN samples. According to the value from XPS spectra and Mott-Schottky analysis, the calculated bandgaps of g-C₃N₄, CCN-0.005, CCN-0.01, CCN-0.03, CCN-0.05 and CCN-0.1 were 2.66, 2.31, 2.24, 2.21, 1.5 and 1.32 eV vs. NHE, respectively. They well agreed with the bandgaps derived from the DRS spectra (Fig. S8). The potentials with reference to the NHE are illustrated in Fig. 2E. It was found that the potentials of pristine g-C₃N₄ and the CCN samples (except CCN-0.1) satisfied the thermodynamical condition for photocatalytic water splitting with hydrogen evolution [54].

In order to understand the relationship between the introduction of cyano group and the narrowed bandgaps of the CCN, density-functional theory calculations (DFT) of density of states (DOS) for pristine g-C₃N₄ and the CCN were performed (Fig. 3A and B). The calculations showed that pristine g-C₃N₄ exhibited a wider band gap than CCN (e.g., CCN-0.03). And when the two C≡N on $-\text{C}-\text{NH}_2$ and $-\text{C}=\text{NH}$ moieties

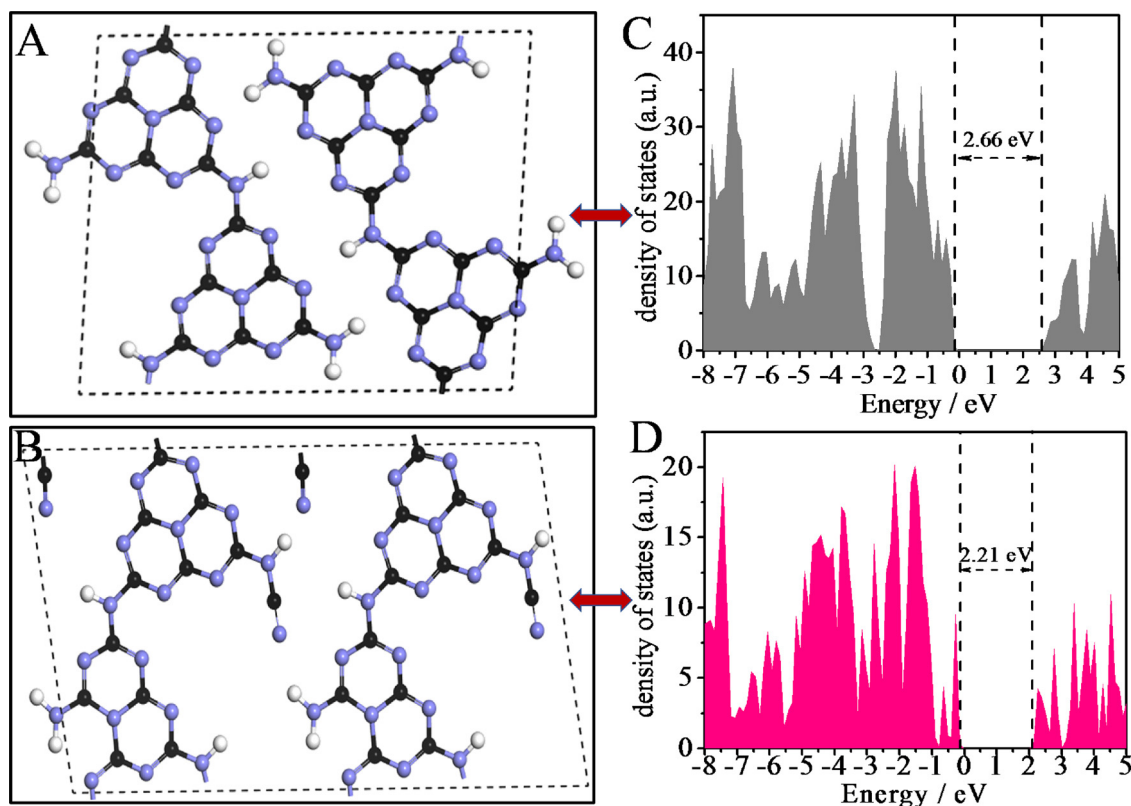


Fig. 3. Structure models of (A) g-C₃N₄ and (B) CCN with different C≡N on –C–NH₂ and –C=NH moieties). Corresponding calculated DOS for (C) g-C₃N₄ and (D) CCN.

coexisted in the same unit cell of g-C₃N₄, the bandgap energy of the CCN decreased (Fig. 3C and D). However, when only one type of C≡N defect was present in one unit cell of CCN, the band gaps firstly become smaller than pristine g-C₃N₄, and then became larger with increasing cyano groups in the unit cell of CCN (Figs. S9 and S10). Moreover, when the number of C≡N defect in one unit cell was above two, the band gaps of CCN were larger than that for pristine g-C₃N₄. In contrast, when two types of C≡N defect in one unit cell of CCN, the band gap was still narrower than that for pristine g-C₃N₄ even if the number of C≡N defect in one unit cell of CCN reached to four (Fig. S11). These results indicated that the narrowed bandgap of CCN compared to pristine g-C₃N₄ should be attributed to the coexistence of two types of cyano defects in the carbon nitride framework.

The introduction of cyano group in g-C₃N₄ would be expected to influence the separation of photoexcited charge carriers, which could be characterized by photoluminescence (PL) spectroscopy, time resolved PL spectroscopy, and the electrochemical impedance spectroscopy (EIS). Pristine g-C₃N₄ showed an intense PL signal (Fig. 4A), indicating the fast recombination of photoinduced charge carriers. In contrast, the signal progressively became weak for CCN samples with more KCl addition during the thermal-polymerization process, indicating that the introduction of cyano group in g-C₃N₄ was highly beneficial for the separation of photoinduced charge carriers in CCN. In addition, the PL peaks showed a gradual red-shift with more KCl addition, meaning narrowed bandgaps. According to the time resolved PL spectra (Fig. 4B), the calculated average PL lifetime (τ) was shortened from 9.10 ns in pristine g-C₃N₄ to 1.86 ns in CCN-0.03 (Table S5). The remarkable shortening of the PL lifetime and related suppression of the radiative recombination should be attributed to the emergence of the band-tails-involved rapid radiative electron-hole recombination processes in CCN-0.03 (Fig. S12). In order to monitor the evolution of the electronic band structure for CCN catalysts, the room-temperature electron paramagnetic resonance (EPR) spectra was recorded (Fig. 4C).

Both pristine g-C₃N₄ and CCN-0.03 exhibited a paramagnetic absorption signal with the *g* value of 2.0034, due to unpaired electrons on sp²-carbon atoms within the π -conjugated aromatic rings [55,56]. Compared with pristine g-C₃N₄, CCN-0.03 showed an enhanced EPR signal. It should be attributed to the redistribution of π -electrons and the introduction of cyano-terminal (C≡N) groups which extended the π -conjugated system of the material [57,58]. The charge transfer properties of pristine g-C₃N₄ and CCN-0.03 were also evaluated using EIS (Fig. 4D). CCN-0.03 presented much smaller charge transfer resistance than pristine g-C₃N₄. The result was consistent with the transient photocurrent measurements (Fig. S13), where the photocurrent of CCN-0.03 was 2.5 times higher than that for pristine g-C₃N₄. Obviously, the introduction of cyano group into g-C₃N₄ should be highly efficient in promoting the charge transfer and separation in the CCN materials, and thus a better photocatalytic performance would be highly anticipated. Meanwhile, we explored computationally whether the two types of cyano groups in the unit cell could increase local fluctuations of the electrostatic potential for enhancing charge separation or not. As an indicator of the possible charge separation tendency, the highest occupied molecular orbit (HOMO)/the lowest unoccupied molecular orbit (LUMO) locations for pristine g-C₃N₄ and CCN were predicted using DFT calculations (Fig. S14). It is observed that the electron-hole pairs could be more efficiently separated in CCN than in pristine g-C₃N₄, thus reducing their recombination and increasing their probability of interfacial charge transfer for the desired redox reaction. These results are similar to semiconductors with a built-in electric field, which could result in better charge separation and hence higher activity [59,60]. Therefore, introducing the two types of cyano groups into carbon nitrides may be a valid strategy for enhancing charge separation.

The photocatalytic H₂ evolution reactions over CCN and pristine g-C₃N₄ with 3 wt% Pt were tested in 15 vol% triethanolamine (TEOA) solution under visible-light irradiation ($\lambda > 420$ nm) at room temperature (Fig. 4E). CCN-0.03 showed the highest HER rate of

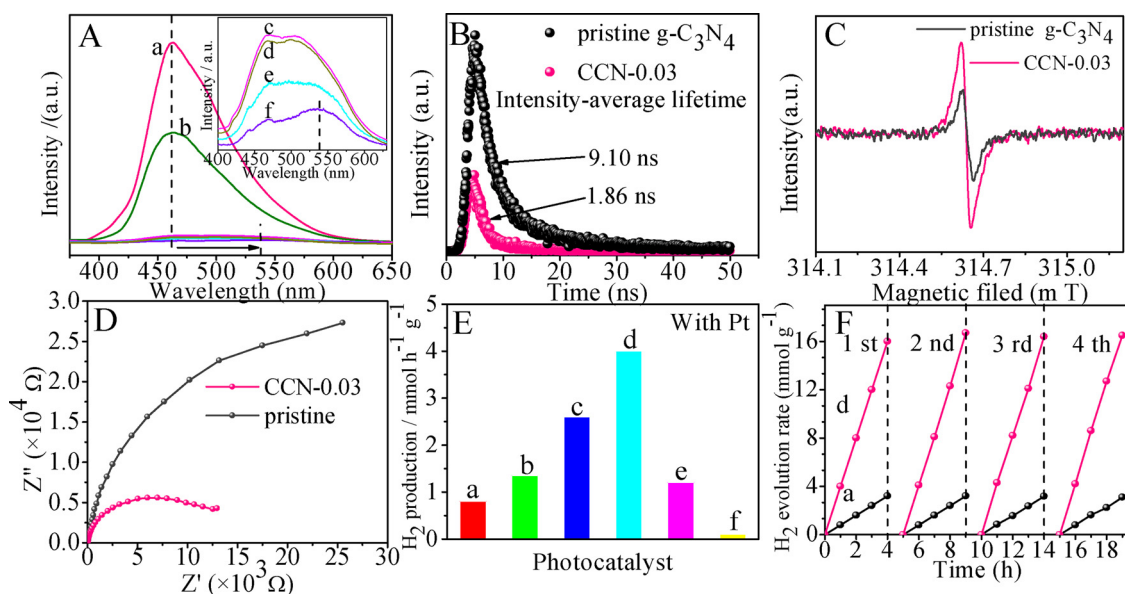


Fig. 4. (A) PL spectra of pristine g-C₃N₄ and CCN samples (excited wavelength of 350 nm). (B) Time-resolved PL decay spectra, (C) room-temperature EPR spectra, and (D) EIS spectra of pristine g-C₃N₄ and CCN-0.03. (E) Photocatalytic hydrogen evolution rates over pristine g-C₃N₄ and CCN photocatalysts with 3 wt% Pt in 15 vol % TEOA aqueous solution under visible-light irradiation ($\lambda > 420$ nm). (F) H₂ evolution cycling over CCN-0.03 and g-C₃N₄. (a) pristine g-C₃N₄, (b) CCN-0.005, (c) CCN-0.01, (d) CCN-0.03, (e) CCN-0.05, and (f) CCN-0.1.

4.0 mmol g⁻¹ h⁻¹, which was 5 times higher than 0.8 mmol g⁻¹ h⁻¹ for pristine g-C₃N₄. As discussed previously, the content of cyano group (C≡N) increased with increasing KCl amount during CCN preparation (Fig. 1B). However, the HER rate did not increase monotonically with increased content of cyano groups. There was an optimal ratio of cyanamide defects at =NH and -NH₂ terminals in CCN for photocatalytic HER activity (e.g., the ratio was 5.1 for CCN-0.03, Table S1). Compared with reported g-C₃N₄ with defects, CCN-0.03 presented an extraordinary HER activity (Table S6). In addition, the HER performance of pristine g-C₃N₄ in this work was better than other reported bare g-C₃N₄, due to its large specific surface area (Table S7).

When in the absence of Pt co-catalysts (Fig. S15), the HER reactivity was closely related to the band energy levels of the photocatalysts (Fig. 2E). CCN-0.03 showed the highest HER rate of 1.6 μmol g⁻¹ h⁻¹, due to the suitable CB energy level closer to (but higher than) the potential of H⁺/H₂. Besides, the HER activity of CCN-0.05 was lower than that for pristine g-C₃N₄, because the CB energy level of CCN-0.05 was nearly equal to the potential of H⁺/H₂ (Fig. 2E), showing a very low reduction driving force for H₂ evolution. In addition, no hydrogen was detected for CCN-0.1, due to the lower CB energy level than the potential of H⁺/H₂ (Fig. 2E). The results further suggest that there was an optimal ratio of cyanamide defects at =NH and -NH₂ terminals in CCN for photocatalytic HER activity. The photocatalytic HER stabilities of pristine g-C₃N₄ and CCN-0.03 were tested (Fig. 4F). Both pristine g-C₃N₄ and CCN-0.03 kept highly stable HER activities after four runs lasting 16 h.

Based on the results above, we could preliminarily infer that a required (although not necessarily sufficient) criterion for photocatalytic HER activity may be attributed to the presence of cyano-terminal as a coordinating group which would provide the ligating linkage to the platinum center to facilitate the transfer of the photoexcited charge from the heptazine core. To confirm the inference, the interactions between the lateral edges of pristine g-C₃N₄ (or CCN) and single Pt atom were modeled by DFT simulations using periodic supercells (Fig. 5A and B). The binding energies were -2.14 eV for pristine g-C₃N₄ and -2.20 eV for CCN. In addition, the DFT simulations of the interactions between the surfaces of pristine g-C₃N₄ (or CCN) and single Pt atom were conducted (Fig. S16). The surface binding energies were 0.77 eV for pristine g-C₃N₄ and -1.04 eV for CCN. These results

indicated the interaction of the pristine g-C₃N₄ and Pt atom was weak and only occurred at the lateral edges of pristine g-C₃N₄ (the surface binding energy of 0.77 eV was positive). In contrast, the interaction of CCN and Pt atom could occur both at the lateral edges and the surface of CCN (the binding energies were negative). It could be explained by the fact that the introduction of cyanamide defects in carbon nitride hindered the inter-molecule hydrogen bonds in carbon nitride, thus releasing more active sites for binding Pt atoms. The spatial distribution of Pt particles on pristine g-C₃N₄ and CCN was illustrated in Fig. 5C and D. The TEM images further confirmed the inference (Fig. 5E and F). The Pt particles remarkably aggregated at the lateral edges of pristine g-C₃N₄ sheet while the Pt particles were distributed at the lateral edges and surfaces of CCN-0.03 sheets. Thus, the electrons produced in CCN could be fast transferred to Pt cocatalysts, resulting in high HER activity. To confirm the wavelength-dependent H₂ evolution over CCN-0.03, the photocatalytic HER activities of CCN-0.03 qualitatively tracked its characteristic absorption (Fig. S17). The HER rate decreased with longer photo-excitation wavelength and the apparent quantum efficiencies were 14.65%, 10.95%, 6.03% and 1.16% at 420, 450, 500 and 550 (± 10 nm), respectively (Table S8).

4. Conclusion

In summary, a facile and effective strategy was explored to synthesize carbon nitride with cyanamide defects through thermal polymerization of thiourea in the presence of KCl. Significantly, two types of cyanamide defects accompanying isomerization of thiourea were introduced and their contents and ratios could be easily adjusted by controlling KCl dosage. The controllable positioning of cyanamide defects greatly improved the binding of co-catalyst Pt. Furthermore, the bandgaps and energy levels of the photocatalysts could be modulated by KCl dosage, thus achieving enhanced HER activity. As far as we know, it is the first report that the molecular tunability route allows in situ synthesis of carbon nitriles with tailored optical and photocatalytic properties without introducing foreign materials or elements.

Acknowledgements

This work was supported by the National Natural Science

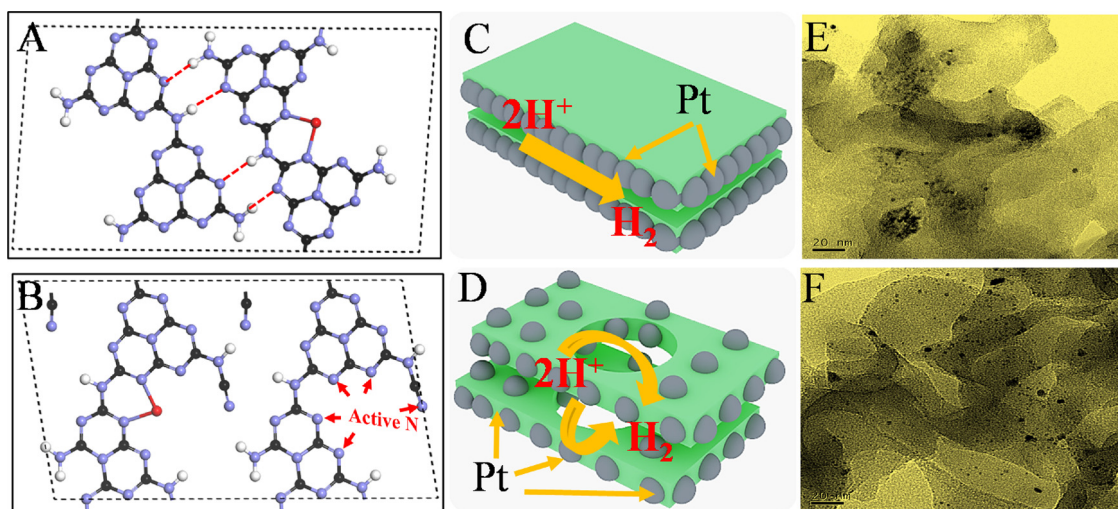


Fig. 5. Structure models of single Pt atom on (A) the lateral edges of pristine g-C₃N₄ and (B) CCN. Schematic spatial distribution of Pt particles on (C) pristine g-C₃N₄ and (D) CCN. TEM images of (E) pristine g-C₃N₄ and (F) CCN-0.03 with deposited Pt nanoparticles.

Foundation of China (51572077, 51778218, 51478171, 21422305 and 21773201). And we do thank the English editing by Professor Xiaorong Zhou at the University of Manchester.

Appendix A. Supplementary data

Supplementary material related to this article can be found, in the online version, at doi:<https://doi.org/10.1016/j.apcatb.2018.05.064>.

References

- [1] X. Zou, Y. Zhang, *Chem. Soc. Rev.* 44 (2015) 5148–5180.
- [2] Z. Zou, J. Ye, K. Sayama, H. Arakawa, *Nature* 414 (2001) 625–627.
- [3] J.H. Montoya, L.C. Seitz, P. Chakthranont, A. Vojvodic, T.F. Jaramillo, J.K. Nørskov, *Nat. Mater.* 16 (2017) 70–81.
- [4] S. Chu, Y. Cui, N. Liu, *Nat. Mater.* 16 (2017) 16–22.
- [5] J.L. Bredas, E.H. Sargent, G.D. Scholes, *Nat. Mater.* 16 (2017) 35–44.
- [6] X. Wang, K. Maeda, A. Thomas, K. Takanabe, G. Xin, J.M. Carlsson, K. Domen, M. Antonietti, *Nat. Mater.* (2011) 271–275.
- [7] J. Zhang, X. Chen, K. Takanabe, K. Maeda, K. Domen, J.D. Epping, X. Fu, M. Antonietti, X. Wang, *Angew. Chem. Int. Ed.* 49 (2010) 441–444.
- [8] S. Docao, A.R. Koirala, M.G. Kim, L.C. Hwang, M.K. Song, K.B. Yoon, *Energy Environ. Sci.* 10 (2017) 628–640.
- [9] P. Niu, L. Zhang, G. Liu, H.M. Cheng, *Adv. Funct. Mater.* 22 (2012) 4763–4770.
- [10] J. Liu, Y. Liu, N. Liu, Y. Han, X. Zhang, H. Huang, Y. Lifshitz, S.T. Lee, J. Zhong, Z. Kang, *Science* 347 (2015) 970–974.
- [11] C. Butchosa, P. Guiglion, M.A. Zwijnenburg, *J. Phys. Chem. C* 118 (2014) 24833–24842.
- [12] B.V. Lotsch, W. Schnick, *Chem. Mater.* 18 (2006) 1891–1900.
- [13] A. Zambon, J.M. Mouesca, C. Gheorghiu, P. Bayle, J. Pécaut, M. Claeys-Bruno, S. Gambaletti, L. Dubois, *Chem. Sci.* 7 (2016) 945–950.
- [14] B.V. Lotsch, W. Schnick, *New J. Chem.* 28 (2004) 1129–1136.
- [15] G. Liu, P. Niu, C. Sun, S.C. Smith, Z. Chen, G.Q. Lu, H.M. Cheng, *J. Am. Chem. Soc.* 132 (2010) 11642–11648.
- [16] Y. Wang, Y. Di, M. Antonietti, H. Li, X. Chen, X. Wang, *Chem. Mater.* 22 (2010) 5119–5121.
- [17] J. Zhang, X. Chen, K. Takanabe, K. Maeda, K. Domen, J.D. Epping, X. Fu, M. Antonietti, X. Wang, *Angew. Chem. Int. Ed.* 49 (2010) 441–444.
- [18] Y. Zhang, T. Mori, J. Ye, M. Antonietti, *J. Am. Chem. Soc.* 132 (2010) 6294–6295.
- [19] Z. Lin, X. Wang, *Angew. Chem. Int. Ed.* 52 (2013) 1735–1738.
- [20] K. Schwinghammer, B. Tuffy, M.B. Mesch, E. Wirnhier, C. Martineau, F. Taulelle, W. Schnick, J. Senker, B.V. Lotsch, *Angew. Chem. Int. Ed.* 52 (2013) 2435–2439.
- [21] J. Zhang, G. Zhang, X. Chen, S. Lin, L. Möhlmann, G. Dolega, G. Lipner, M. Antonietti, S. Blechert, X. Wang, *Angew. Chem. Int. Ed.* 124 (2012) 3237–3241.
- [22] X. Chen, Y.S. Jun, K. Takanabe, K. Maeda, K. Domen, X. Fu, M. Antonietti, X. Wang, *Chem. Mater.* 21 (2009) 4093–4095.
- [23] J. Sun, J. Zhang, M. Zhang, M. Antonietti, X. Fu, X. Wang, *Nat. Commun.* 3 (2012) 1139–1140.
- [24] X. Wang, K. Maeda, X. Chen, K. Takanabe, K. Domen, Y. Hou, X. Fu, M. Antonietti, *J. Am. Chem. Soc.* 131 (2009) 1680–1681.
- [25] W.J. Ong, L.L. Tan, S.P. Chai, S.T. Yong, A.R. Mohamed, *Nano Energy* 13 (2015) 757–770.
- [26] Z. Zhao, Y. Sun, F. Dong, *Nanoscale* 7 (2015) 15–37.
- [27] A. Vojvodic, J.K. Nørskov, *Natl. Sci. Rev.* 2 (2015) 140–143.
- [28] V.W.h. Lau, I. Moudrakovski, T. Botari, S. Weinberger, M.B. Mesch, V. Duppel, J. Senker, V. Blum, B.V. Lotsch, *Nat. Commun.* 7 (2016) 12165.
- [29] G. Liu, G. Zhao, W. Zhou, Y. Liu, H. Pang, H. Zhang, D. Hao, X. Meng, P. Li, T. Kako, *Adv. Funct. Mater.* 26 (2016) 6822–6829.
- [30] H. Yu, R. Shi, Y. Zhao, T. Bian, Y. Zhao, C. Zhou, G.I. Waterhouse, L.Z. Wu, C.H. Tung, T. Zhang, *Adv. Mater.* 29 (2017) 1605148.
- [31] V.W.h. Lau, V.W.z. Yu, F. Ehrat, T. Botari, I. Moudrakovski, T. Simon, V. Duppel, E. Medina, J. Stolarczyk, J. Feldmann, V. Blum, B.V. Lotsch, *Adv. Energy Mater.* 7 (2017) 16002251.
- [32] A. Thomas, A. Fischer, F. Goettmann, M. Antonietti, J.O. Müller, R. Schlögl, J.M. Carlsson, *J. Mater. Chem.* 18 (2008) 4893–4908.
- [33] B.V. Lotsch, M. Döblinger, J. Schnert, L. Seyfarth, J. Senker, O. Oeckler, W. Schnick, *Chem. Eur. J.* 13 (2007) 4969–4980.
- [34] F. Fina, S.K. Callear, G.M. Carins, J.T. Irvine, *Chem. Mater.* 27 (2015) 2612–2618.
- [35] E. Irran, B. Jürgens, W. Schnick, *Solid State Sci.* 4 (2002) 1305–1311.
- [36] W. Lei, D. Portehault, R. Dimova, M. Antonietti, *J. Am. Chem. Soc.* 133 (2011) 7121–7127.
- [37] Y. Cui, Z. Ding, X. Fu, X. Wang, *Angew. Chem. Int. Ed.* 51 (2012) 11814–11818.
- [38] H. Gao, S. Yan, J. Wang, Y.A. Huang, P. Wang, Z. Li, Z. Zou, *Phys. Chem. Chem. Phys.* 15 (2013) 18077–18084.
- [39] E. Irran, B. Jürgens, S. Schmid, W. Schnick, *Z. Anorg. Allg. Chem.* 631 (2005) 1512–1515.
- [40] B. Jürgens, E. Irran, J. Senker, P. Kroll, H. Müller, W. Schnick, *J. Am. Chem. Soc.* 125 (2003) 10288–10300.
- [41] S.J. Makowski, D. Gunzelmann, J. Senker, W. Schnick, *Z. Anorg. Allg. Chem.* 635 (2009) 2434–2439.
- [42] H. Ou, P. Yang, L. Lin, M. Anpo, X. Wang, *Angew. Chem. Int. Ed.* 28 (2017) 10905–10910.
- [43] J. Liu, T. Zhang, Z. Wang, G. Dawson, W. Chen, *J. Mater. Chem.* 21 (2011) 14398–14401.
- [44] F. Dong, Z. Zhao, T. Xiong, Z. Ni, W. Zhang, Y. Sun, W.K. Ho, *ACS Appl. Mater. Interface* 5 (2013) 11392–11401.
- [45] T. Sano, S. Tsutsui, K. Koike, T. Hirakawa, Y. Teramoto, N. Negishi, K. Takeuchi, *J. Mater. Chem. A* 1 (2013) 6489–6496.
- [46] P. Niu, L.C. Yin, Y.Q. Yang, G. Liu, H.M. Cheng, *Adv. Mater.* 26 (2014) 8046–8052.
- [47] Y. Kang, Y. Yang, L.C. Yin, X. Kang, L. Wang, G. Liu, H.M. Cheng, *Adv. Mater.* 28 (2016) 6471–6477.
- [48] Y.S. Jun, E.Z. Lee, X. Wang, W.H. Hong, G.D. Stucky, A. Thomas, *Adv. Funct. Mater.* 23 (2013) 3661–3667.
- [49] S. Yang, Y. Gong, J. Zhang, L. Zhan, L. Ma, Z. Fang, R. Vajtai, X. Wang, P.M. Ajayan, *Adv. Mater.* 25 (2013) 2452–2456.
- [50] Y. Cao, Z. Zhang, J. Long, J. Liang, H. Lin, H. Lin, X. Wang, *J. Mater. Chem. A* 2 (2014) 17797–17807.
- [51] W. Zhou, W. Li, J.-Q. Wang, Y. Qu, Y. Yang, Y. Xie, K. Zhang, L. Wang, H. Fu, D. Zhao, *J. Am. Chem. Soc.* 136 (2014) 9280–9283.
- [52] Z. Hong, B. Shen, Y. Chen, B. Lin, B. Gao, *J. Mater. Chem. A* 1 (2013) 11754–11761.
- [53] S. Trasatti, *Pure Appl. Chem.* 58 (1986) 955–966.
- [54] J. Zhang, M. Grzelczak, Y. Hou, K. Maeda, K. Domen, X. Fu, M. Antonietti, X. Wang, *Chem. Sci.* 3 (2012) 443–446.
- [55] G. Zhang, M. Zhang, X. Ye, X. Qiu, S. Lin, X. Wang, *Adv. Mater.* 26 (2014) 805–809.
- [56] M. Tabbal, T. Christidis, S. Isber, P. Merel, M. El Khakani, M. Chaker, A. Amassian, L. Martinu, *J. Appl. Phys.* 98 (2005) 044310.
- [57] J. Zhang, M. Zhang, S. Lin, X. Fu, X. Wang, *J. Catal.* 310 (2014) 24–30.
- [58] J. Zhang, M. Zhang, R.Q. Sun, X. Wang, *Angew. Chem. Int. Ed.* 124 (2012) 10292–10296.
- [59] S. Park, C.W. Lee, M.-G. Kang, S. Kim, H.J. Kim, J.E. Kwon, S.Y. Park, C.Y. Kang, K.S. Hong, K.T. Nam, *Phys. Chem. Chem. Phys.* 16 (2014) 10408–10413.
- [60] L. Li, P.A. Salvador, G.S. Rohrer, *Nanoscale* 6 (2014) 24–42.